Universidade do Minho
Escola de Engenharia

Ana Jorge Rodrigues de Moura Leitão

Analysis of the Myocardial Function using Tagging MR

outubro de 2013

Ana Jorge Rodrigues de Moura Leitão **Analysis of the Myocardial Function using Tagging MR**

UMinho | 2013

Universidade do Minho
Escola de Engenharia

Ana Jorge Rodrigues de Moura Leitão

Analysis of the Myocardial Function using Tagging MR

Dissertação de Mestrado
Mestrado Integrado em Engenharia Biomédica
Ramo de Engenharia Informática Médica

Trabalho efetuado sob a orientação do
Professor Victor Manuel Rodrigues Alves

outubro de 2013

Acknowledgments

I would like to thank Prof. Dr. L.M.J. Florack for giving me the opportunity to go to the Netherlands and to the TU/e allowing me to live a new experience and to grow and build up professionally and personally.

To Dr. Andrea Fuster for the support, disposability, optimism and guidance given along this year.

To my friends and colleagues specially João Loureiro, that supported me and made some long weeks in Eindhoven bearable.

To my family for all the support, specially to my brother Filipe for believing in me and making me believe that I am capable of doing more than I ever thought.

I thank mostly to my parents for sacrificing a lot for me, for pushing me and for being there every time I needed.

Finally, to Antonio, who was there in all the moments and without whom I wouldn't have last this long so far way from home.

Abstract

Heart diseases can often manifest themselves by irregularities in the movement of the heart muscle. To assess the function of the myocardium, a method based in the Optic Flow Constrain Equation (OFCE) is applied in tagging MR images. The sequence of tagging MR images allows us to detect deviations in deformation and strain through time. However, the application of the OFCE implies the assumption of spatial phase conservation. Therefore, harmonic filters in the Fourier domain were used in each frame of the sequence to remove the variation of intensity trough time.

In order to achieve a model capable of distinguishing a malfunction from normal function of the cardiac wall it is necessary to acknowledge what is the ground truth and which factors can affect the results. This study explores several scenarios using synthetic data that mimic tagged MR images in order to discover which variables can optimize the OFCE.

This work allows us to analyze up to what extension the OFCE can be applied to a cardiac motion simulator (CMS) based on Waks et al. [1], capable of reproducing the normal function of the heart. After a series of tests with simulated data and the respective comparison with real volunteers data, it is possible to assess quantitatively the method used.

Resumo

Grande parte das doenças cardíacas estão associadas a um consequente mau funcionamento dos músculos cardíacos. Sendo que o músculo cardíaco maior e do qual depende o funcionamento do coração é o miocárdio, torna-se relevante quantificar a deformação do mesmo. Esta quantificação permite calcular o volume do sangue que é bombeado por ciclo cardiaco e a fracção de ejecção cardíaca. Neste trabalho propoem-se a aplicação de um método que utiliza a "Optic Flow Constrain Equation"(OFCE), a imagens de ressonância magnética (RM) marcadas. A sequencia de imagens the RM marcadas permite-nos detectar desvios na deformação e tensão no tempo. No entanto, o uso da OFCE implica que se assuma a existência de conservação de fase. Para tal, para remover a variação de intensidade no tempo, foram aplicados filtros no domínio de Fourier a cada uma das imagens da sequência.

Para atingir um modelo capaz de distinguir um funcionamento anormal do miocárdio é necessário saber o que significa numéricamente o comportamento normal de um músculo saudável e quais os factores que podem afectar a sua quantificação. Este estudo baseia-se na simulação de cenários para determinar que variáveis podem ajudar a optimização do método com OFCE.

Este trabalho permite analizar a aplicabilidade da OFCE a um simulador de movimento cardíaco (SMC), baseado no trabalho de Waks et al. [1], capaz de reproduzir o movimento normal do coração. Depois do estudo intensivo das várias simulações e respectiva comparação com dados reais, é possível avaliar quantitativamente o método utilizado.

Contents

List of Figures

List of Tables

List of Acronyms

CMS	Cardiac Motion Simulator
(C)SPAMM	Complementary Spatial Modulation of Magnetization
CVD	Cardiovascular Diseases
DENSE	Displacement Encoding with Stimulated Echoes
HARP	Harmonic Phase Imaging
LA	Long Axis
LV	Left Ventricle
MR	Magnetic Resonance
OFCE	Optic Flow Constrain Equation
PC-MRI	Phase Contrast Magnetic Resonance Image
RoI	Region of Interest
SA	Short Axis
TD	Tissue Doppler

Chapter 1

Introduction

Cardiovascular diseases (CVD) are the main cause of mortality in the world. In the year 2012, they represented 47% of the cause of deaths in Europe and 40% in the US [4]. Everyday life habits such as smoking, diet, physical activity or even other diseases like obesity and diabetes can be the cause of heart diseases.

According to the Frank-Starling relation, the strength of the pump function of the heart is proportional to the distention of the myocardium. This means that any diseases that decrease the myocardium's capacity to distend or that cause a higher distention, affect the blood flow in the human body. Therefore, the study and quantification of the myocardium motion can become a relevant step in preventing CVD. Despite the fact that the myocardium extends itself through both ventricles in this work only the left ventricle (LV) is taken in consideration. This decision was based on the fact that the LV is responsible for the transport of the arterial blood to the aorta and consequently to the entire body, as is presented in Figure 1.1. Also, the majority of cardiovascular diseases influence the interior walls of the heart diminishing the myocardium capacities hence affecting the movement and pump function of the LV.

One of the imaging techniques that allow us to visualize the interior of the heart is Magnetic Resonance (MR). Nonetheless with MR we are only able to distinguish the different tissues by calculating their times of relaxation (explained in Chapter 2). Which means that

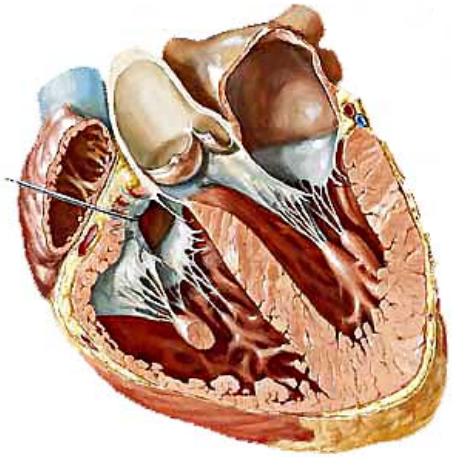

Figure 1.1: Netter's image of the heart with LV on the right [2].

the interior of the heart wall appear has a whole. A useful way to assess intramyocardial movement is the use of tagging MR.

By the use of magnetic spatial modulation, an artificial brightness pattern is created. This pattern is represented by black stripes superimposed on the original MR images. However the tagging images can only solve the problem of visualization. To quantify the motion of the left ventricle a method based in the classical optical flow method in the spectral domain is applied. In order to solve the optical flow constrain equation (OFCE) without the necessity of additional constrains we apply the method described by Florack et al. [5], which makes use of two tagging MR image sequences simultaneously. These two sequences are obtained in the same temporal space and for the same movement but have different tag patterns (one has horizontal patterns and the other vertical patterns, see Figure 1.2). However, the assumption that there is no loss of pixel brightness has to be made. In the end is finally possible to quantify the motion, deformation and strain of the heart muscle.

Nonetheless, no quantification is relevant if there is no ground truth to compare to. In this work, a quantification and validation of the method explained above is proposed. This is accomplished by comparing the results calculated using the OFCE, with synthetic data

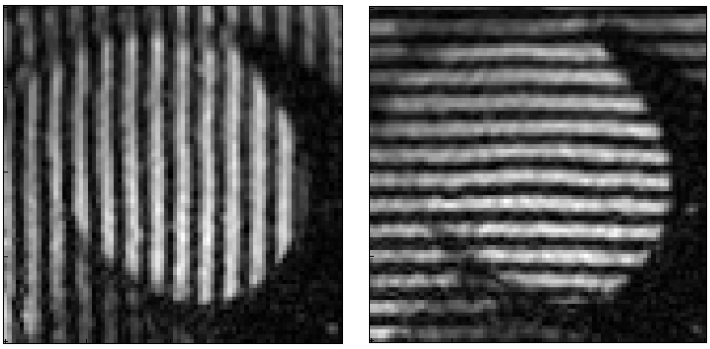

(a) (b)

Figure 1.2: Short axis MR images of the left ventricle with (a) vertical tag pattern and (b) horizontal tag pattern.

produced by a model of the left ventricle based on the work of Waks et al. [1].

1.1 Test methodology

All the methods and tests described in this work required the use of the computational software program Mathematica 9, from Wolfram Research. The choice of the program was made taking in consideration the software licenses owned by the Technical University of Eindhoven, where this work was developed, and the compatibility with the work already done on the topic and possible extensions to this work to be made in the future.

1.2 Dissertation layout

This work is divided in five chapters. Throughout the first chapter are explained the basic ideas that led us to this study. As well as the basic knowledge necessary to understand the practical work presented in the following chapters. In the same chapter is also presented some useful information on synthetic and real data from MR images. In chapter three the analysis of the factors that can affect velocity is made. Chapter four explores the presence of noise in MR images and the effect that this can have in the factors studied in chapter

three. Finally in chapter five the conclusions of this study are presented as well as the future work that can be done.

Chapter 2

Background

2.1 Tagging MR

Magnetic Resonance (MR) is a noninvasive technique used mainly in medicine to produce high quality images of the human organs. This technique is based in the interaction between radio frequency pulses with a strong magnetic field and the water molecules of the human body. During the procedure the patient is introduced in a cylindric scanner that produces a high magnetic field such as 1.5 up to 9.4 Tesla. The magnetic field produced by the machine is capable of realigning the magnetic moments of hydrogen protons and, by imposing a radio frequency signal usually perpendicular to the machine's magnetic field, the protons rise to a higher energy level. When the radio frequency signal is turned off the hydrogen protons return to their original alignment with a particular relaxation time. The energy released on the decay of the realignment produces a signal detectable by the machine. As known, the human body is primarily water distributed in distinct ways in different tissues. Therefore each tissue has a distinct relaxation time producing a different level of contrast in MR images.

Magnetic Resonance cardiac images can be obtained in two different views: long axis (LA) that divides the heart in vertical sections (parallel to the axis of the left ventricle) and the short axis (SA) perpendicular to the LA that gives us horizontal sections of the heart

from apex to the base.

Despite of the contrast between tissues obtained by magnetic resonance, MR becomes useless in the case of motion evaluation of the inside of a particular tissue. In 1988 a new technique called “tagging" for visualization of the intramyocardial motion with MR was introduced by Zerhouni et al. [6]. This method locally saturates the magnetization of the tissue and it results in lines or grids in the final MR image. On the other hand, due to the influence of longitudinal relaxation of the magnetization the tagging information decays restricting the application of these methods. This phenomena it is called tag fading.

In 1993, Fischer et al. [7] proposed a modification to Zerhouni's technique. The (C)SPAMM (complementary spatial modulation of magnetization) allows access to systolic and diastolic motion data guaranteeing that the tagging pattern remains constant during the whole cardiac cycle. This method also grants the possibility to analyse local dynamic behavior of deformation and strain in the LV by creating patterns inherent in the tissue.

2.1.1 Extraction of Phase Images from tagging MR

In the late 1990's a new approach to the analysis of tagged MR images called HARP (harmonic phase imaging) was introduced by Osman et al. [8]. This approach applies tagging combined with spectral filtering in k-space and by directly measuring phase information of the MR signal, it overcomes the problem of tag fading.

Following the idea of phase-based algorithms, in 1999 the DENSE (displacement encoding with stimulated echoes) method [9] and later the imaging protocol for dynamic analysis called Phase Contrast MRI (PC-MRI) were introduced [10].

The HARP method uses bandpass filters to isolate k-th spectral peaks in SPAMM-tagged magnetic resonance images, centered at a certain frequency. After the most suitable filter is selected and applied to each image of the sequence given as a result of the tagging MR, the inverse Fourier transform of the bandpass region yields a complex harmonic im-

age, given by

$$I_k(y,t) = D_k(y,t)e^{j\phi_k(y,t)} \tag{2.1}$$

where D_k is the harmonic magnitude image and ϕ_k is the harmonic phase image. Given ϕ_k is possible to compute a_k known has the harmonic phase angle, in Equation 2.2.

$$a_k(y,t) = W(\phi_k(y,t)), \tag{2.2}$$

and the nonlinear wrapping function is given by

$$W(\phi) = mod(\phi + \pi, 2\pi) - \pi. \tag{2.3}$$

In a second stage of the method the harmonic phase angle image is used to track the phases. After the application of the HARP method to the tagged MR images (Figure 1.2) we obtain the result shown in Figure 2.1.

The HARP method serves as a basis for the OFCE approach explained in Section 2.2.

2.2 Optic Flow

Following the idea described by Barron et al. [11] optic flow theories can be divided in three main types: differential methods, correlation methods and frequency domain methods. The main goal of these methods is to detect apparent motion by extracting the velocity of moving patterns in image sequences. Nowadays, the methods are not as simple to define in types nonetheless the OFCE developed by Florack et al. [5] is mainly based in the differential techniques presented in Section 2.2.1.

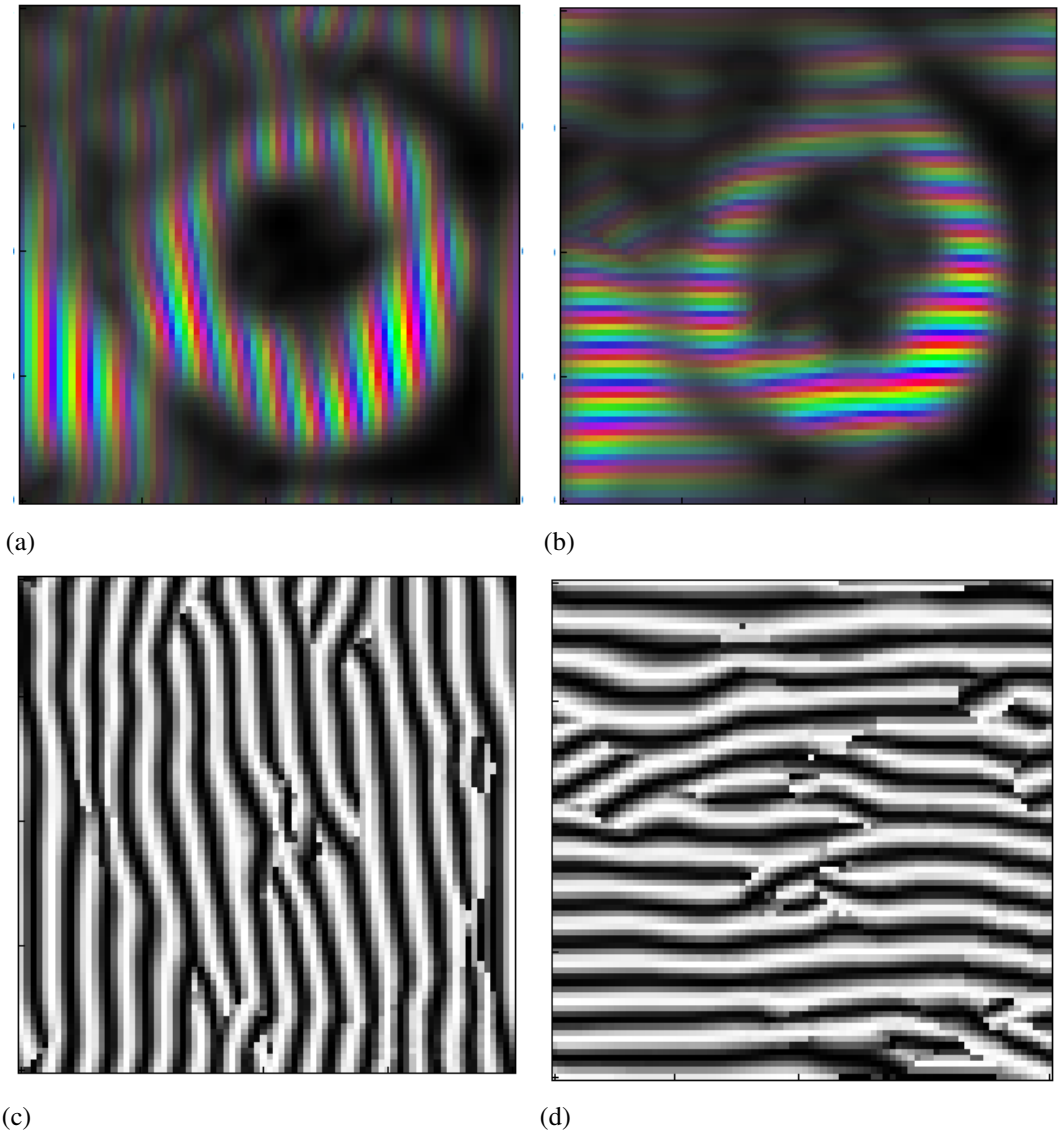

(a) (b)

(c) (d)

Figure 2.1: Harmonic phase (HARP) images of :(a) vertically tagged MR image in short axis of the left ventricle and (b) horizontally tagged MR image in short axis of the left ventricle. (c),(d): Sine of the HARP images in (a) and (b) respectively.

2.2.1 Differential Techniques

Differential Techniques use image intensity or filtered versions of the image to assess the velocity by computing spatiotemporal derivatives. However, the assumption that there is no pixel brightness decay, has to be made. Given an image sequence $f(x, y, t) : \Re^2 \times \Re^+ \rightarrow \Re$, where x, y and t represent the spatial and temporal coordinates

$$f(x + \delta x, y + \delta y, t + \delta t) = f(x, y, t) \tag{2.4}$$

and δx, δy, δt represent the displacement in space and time. After applying the Taylor's series in the left hand side of the previous equation we have the basic Optic Flow Constrain Equation (OFCE)

$$\frac{\partial f}{\partial x}\frac{\delta x}{\delta t} + \frac{\partial f}{\partial y}\frac{\delta y}{\delta t} + \frac{\partial f}{\partial t} = 0 \Leftrightarrow f_x u + f_y v + f_t = 0 \tag{2.5}$$

where u and v are the velocities in the x and y direction. This equation, however, presents itself with a problem called "aperture problem". The problem resumes in the fact that u and v are both unknown variables and so Equation 2.5 has no unique solution. The usual way to overcome the "aperture problem" is to complement our data with prior knowledge or by making an assumption about the true motion field. According with Horn et al. [12] the physical motion fields tend to get smoother due to inertial and coherence of physical objects. Therefore, they introduced a new term in Equation 2.5 obtaining the regularized optic flow technique

$$\int\limits_{\Omega \subset \Re^2} \left[(f_x u + f_y v + f_t)^2 + \lambda(|\nabla u|^2 + |\nabla v|^2) \right] dxdy \tag{2.6}$$

where ∇ is the gradient and λ is a positive weight that leads to a smoother velocity field when given large values. Nevertheless if the motion field presents strong variations it will not be retrieved correctly.

A multiscale generalization of this model was proposed by Florack et al. [13], Niessen

et al. [14][15] and Suinesiaputra et al. [16]. In this new method conditions that reflected known facts about simulated object dynamics were imposed. Their success was based in the use of spatial and temporal scale degrees of freedom (d.o.f.'s) of Gaussian derivative filters. An assumption that the source data forms a scalar field is made. Therefore, given an image $f_0(x, y, t)$ where x, y and t are spatial and temporal coordinates by convolution with a derivative of a normalized Gaussian

$$\phi(x, y, t; \sigma, \tau) = \frac{1}{2\pi\sigma^2\sqrt{2\pi\tau^2}} e^{-\frac{x^2+y^2}{2\sigma^2}-\frac{t^2}{2\tau^2}} \tag{2.7}$$

we obtain a scale space representation f

$$f(x, y, t, \sigma, \tau) = f_0(x, y, t) * \phi(x, y, t; \sigma, \tau) \tag{2.8}$$

where $\sigma > 0$ and $\tau > 0$ represent the isotropic spatial scale and the temporal scale respectively.

The optic flow scheme uses a local polynomial expansion of the velocity field, in every point, up to a certain order. For a first order scheme, the two components of the velocity field are $U(x, y, t) = u + u_x x + u_y y + u_t t$ and $V(x, y, t) = v + v_x x + v_y y + v_t t$. Equation 2.5 can now be represented by a system of matrices

$$Av = a \tag{2.9}$$

A=

$$\begin{bmatrix} f_x & f_y & f_{xt}\tau^2 & f_{yt}\tau^2 & f_{xx}\sigma^2 & f_{xy}\sigma^2 & f_{xy}\sigma^2 & f_{yy}\sigma^2 \\ f_{xt} & f_{yt} & f_x + f_{xtt}\tau^2 & f_y + f_{ytt}\tau^2 & f_{xxt}\sigma^2 & f_{xyt}\sigma^2 & f_{xyt}\sigma^2 & f_{yyt}\sigma^2 \\ f_{xx} & f_{xy} & f_{xxt}\tau^2 & f_{xyt}\tau^2 & f_x + f_{xxx}\sigma^2 & f_y + f_{xxy}\sigma^2 & f_{xxy}\sigma^2 & f_{xyy}\sigma^2 \\ f_{xy} & f_{yy} & f_{xyt}\tau^2 & f_{yyt}\tau^2 & f_{xxy}\sigma^2 & f_{xyy}\sigma^2 & fx + f_{xyy}\sigma^2 & f_y + f_{yyy}\sigma^2 \end{bmatrix},$$

$$v = [uvu_tv_tu_xv_xu_yv_y]^T \text{ and } a = -[f_t f_{tt} f_{xt} f_{yt}]^T.$$

In order to retrieve the missing d.o.f.'s, Florack et al. [5] added more intrinsic evidence to the one already existing by using a second independent recording of the same spatiotemporal region of interest. This improved method uses two MR image sequences with distinct tagging patterns. We now have a second image sequence g that after the convolution can be represented by

$$Bv = b. \tag{2.10}$$

Assuming that f and g are truly independent we have

$$Cv = c \tag{2.11}$$

where $C = \left[\begin{smallmatrix} A \\ B \end{smallmatrix}\right]$, $c = \left[\begin{smallmatrix} a \\ b \end{smallmatrix}\right]$ and the only possible solution is v. Having this, the "aperture problem" ceases to exist.

2.2.2 3D OFCE

In this work will be analysed 3D MR images, therefore it is necessary to apply a method adapted to this conditions. Taking in consideration the OFCE explained below is then possible to use it in a 3D environment. Having that, we would have a third image h with dimension z and velocity w. The vectors U, V and W would then be

$$\begin{aligned} U(x,y,z,t) &= u + u_x x + u_y y + u_z z + u_t t \\ V(x,y,z,t) &= v + v_x x + v_y y + v_z z + v_t t \\ W(x,y,z,t) &= w + w_x x + w_y y + w_z z + w_t t \end{aligned} \tag{2.12}$$

Consequently, the matrices involved in Equation (2.9) are

$$A = \begin{bmatrix} f_x & f_y & f_z & f_{xt}\tau^2 & f_{xx}\sigma^2 & f_{xy}\sigma^2 & f_{xz}\sigma^2 & f_{yt}\tau^2 & f_{xy}\sigma^2 & f_{yy}\sigma^2 & f_{yz}\sigma^2 & f_{zt}\tau^2 & f_{xz}\sigma^2 & f_{yz}\sigma^2 & f_{zz}\sigma^2 \\ f_{xx} & f_{xy} & f_{xz} & f_{xxt}\tau^2 & f_x + f_{xxx}\sigma^2 & f_{xxy}\sigma^2 & f_{xxz}\sigma^2 & f_{xyt}\tau^2 & f_y + f_{xxy}\sigma^2 & f_{xyy}\sigma^2 & f_{xyz}\sigma^2 & f_{xzt}\tau^2 & f_z + f_{xxz}\sigma^2 & f_{xyz}\sigma^2 & f_{xzz}\sigma^2 \\ f_{xy} & f_{yy} & f_{yz} & f_{xyt}\tau^2 & f_{xxy}\sigma^2 & fx + f_{xyy}\sigma^2 & f_{xyz}\sigma^2 & f_{yyt}\tau^2 & f_{xyy}\sigma^2 & f_y + f_{yyy}\sigma^2 & f_{yyz}\sigma^2 & f_{yzt}\tau^2 & f_{xyz}\sigma^2 & f_z + f_{yyz}\sigma^2 & f_{yzz}\sigma^2 \\ f_{xz} & f_{yz} & f_{zz} & f_{xzt}\tau^2 & f_{xxz}\sigma^2 & f_{xyz}\sigma^2 & fx + f_{xzz}\sigma^2 & f_{yzt}\tau^2 & f_{xyz}\sigma^2 & f_{yyz}\sigma^2 & f_y + f_{yzz}\sigma^2 & f_{zzt}\tau^2 & f_{xzz}\sigma^2 & f_{yzz}\sigma^2 & f_z + f_{zzz}\sigma^2 \\ f_{xt} & f_{yt} & f_{zt} & f_x + f_{xtt}\tau^2 & f_{xxt}\sigma^2 & f_{xyt}\sigma^2 & f_{xzt}\sigma^2 & f_y + f_{ytt}\tau^2 & f_{xyt}\sigma^2 & f_{yyt}\sigma^2 & f_{yzt}\sigma^2 & f_z + f_{ztt}\tau^2 & f_{xzt}\sigma^2 & f_{yzt}\sigma^2 & f_{zzt}\sigma^2 \end{bmatrix}$$

$$v = [uvwu_tv_tw_tu_xv_xw_xu_yv_yw_yu_zv_zw_z]^T \text{ and } a = -[f_tf_{xt}f_{yt}f_{zt}f_{tt}]^T.$$

Following the same arguments given in section 2.2.1, after convolution, image h is represented by

$$Dv = d \tag{2.13}$$

Which means that Equation (2.11) is now

$$Cv = c \tag{2.14}$$

$$\begin{bmatrix} A \\ B \\ D \end{bmatrix} v = \begin{bmatrix} a \\ b \\ d \end{bmatrix} \tag{2.15}$$

2.3 Expected values of Velocity

The assessment of the velocities of the myocardium movement can also help to understand the limitations and constrains of the OFCE. Therefore, it is important to know what range of values are expectable to be detected in a tagged MR sequence of images. As it was mentioned before this kind of knowledge can't be directly obtained with MR, nonetheless there are other imaging techniques capable of detect and analyze the movement of a certain moving target.

The most common imaging technique used to obtain the velocities of the movement of the heart is Tissue Doppler (TD). Manouras et al. [17] used spectral TD, color TD and M-mode recordings to determine the longitudinal systolic myocardial velocities and displacement of the LV. For that study the basal septal and lateral wall of 24 healthy individuals were analyzed. After comparing the results of the 3 different methods, the range of velocities obtained for the myocardium was $[7, 12]\ cm/sec$ and the respective displacement was $[9, 19]\ mm$.

Considering a typical MR image resolution of $1.3 \times 1.3\ mm^2$ and that, per each second approximately 30 frames are obtained it is possible to convert the velocities to pixel/frame. By direct calculation we would then obtain a minimum velocity of $1.846\ pixels/frame$ and a maximum velocity of $3.07\ pixels/frame$. Whereas the displacements would be in the range $[6.92, 14.61]\ pixels$. These resolution values are based on real tagging MR data obtained from anonymous volunteers.

After knowing the range of values that are expected, it is possible to evaluate the limitations of this method.

Chapter 3

Analysis of the Factors Affecting Velocity

For every method or theory there is a range of values and situations for which these are valid and possible to apply. The 3D OFCE method exposed in this work is no exception. Therefore, in order to test the conditions in which this method is reliable, a study of possible combinations of variables was made.

To evaluate and quantify the accuracy of the results obtained, it is necessary to distinguish the factors that influence this method. The knowledge of the consequence of variables such as the width of the tag, the values of σ and τ and also the effect of the boundaries are fundamental. Allowing the possibility of a better manipulation of a specific group of given data and consequently the optimization of the results.

In order to analyze all the factors mentioned above, we create a phantom image that simulates a constant and unidirectional movement. The main idea behind this simulation is to test the system in the simplest case, assuming that if the method fails, it will most likely fail in more complex situations.

To recreate the tag patterns, a sinusoidal function was used. Following the symbology

used in Section A.2 the intensity of each pixel is given by

$$\mu = \sin \frac{2\pi}{L} \left(a(x - ut) + b(y - vt) + c(z - wt)\right) \tag{3.1}$$

In Equation (3.1) L represents the period of the function, t is the time, x, y and z are the coordinates of the pixels, u, v and w are constant velocities imposed to the system and a, b and c represent the unit vector of the movement, $a^2 + b^2 + c^2 = 1$, that allows us to consider any type of movement (unidirectional or oblique). By applying the functions presented above simultaneously, it is possible to simulate a sequence of images were the velocity of the movement can be easily manipulated.

In contrast with Equation (A.7) that uses a tag pattern grid, Equation (3.1) uses three distinct tag patterns and so it is represented as a sum and not a product of the different unidirectional movements.

In a perfect system, when a mathematical method is used to calculate the velocities of the movement created by μ, the final values obtained would be u, v and w. However, this is a unrealistic expectation considering that the input given to the method is not a continuous function, but a sequence of images. As follows, the input for the OFCE is a $3D$ matrix where the movement of the myocardium is represented by the change in pixel intensity frame by frame. Every factor that modifies the pixel value will directly modify the accuracy of the results.

3.1 Image Boundaries

Just like any other method of image analysis that uses convolutions with extended kernels, the OFCE generates artifacts in the boundaries of the image. These artifacts are due to repetitive convolutions in the spatial and temporal domain. The cyclic nature of the method creates a strong edge by neighboring pixels at the ends of the image. Unfortunately there is no way to eliminate the artifacts therefore, a decision in how to deal with this problem has to be made [18].

As a matter of convenience it was decided that the better solution would be to define a section of artifacts and remove it. This decision was based on the fact that the input images used in this work are a section of Thoracic Tagging MR images (see Figure 3.1). Having that, it is easy to manipulate the dimension of the image and the section to be removed without affecting relevant data.

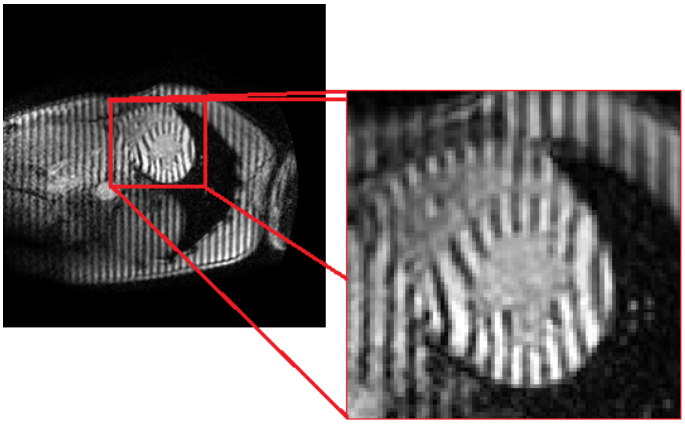

Figure 3.1: Original Thoracic Tagged MR image from anonymous patient (on the left) and analyzed section of the heart (on the right).

It is then necessary to define where is the heart information and remove a section from the Thoracic MR image taking in consideration the area for the artifacts.

Taking in consideration an input image $\mu(x, y, z)$ of dimensions $\{D, D, D\}$ the heart will be in a region of interest RoI$\{x, y, z\} = \{D_{RoI}, D_{RoI}, D_{RoI}\}$. The relation between the two dimensions will be defined by

$$D_{RoI} = D - 2\lambda\sigma \tag{3.2}$$

where σ is the spatial scale used for the kernel convolutions and λ is a constant. For a better comprehension of what is the RoI this was synthesized in Figure 3.2.

In the tests presented in this work, the dimension D used was $20\ pixels$ and λ was set to 2, meaning that $D_{RoI} = 12$. Nonetheless, the boundaries effect tend to be worst with the increase of D so the value of λ as to be increased. Thus is necessary to find a balance

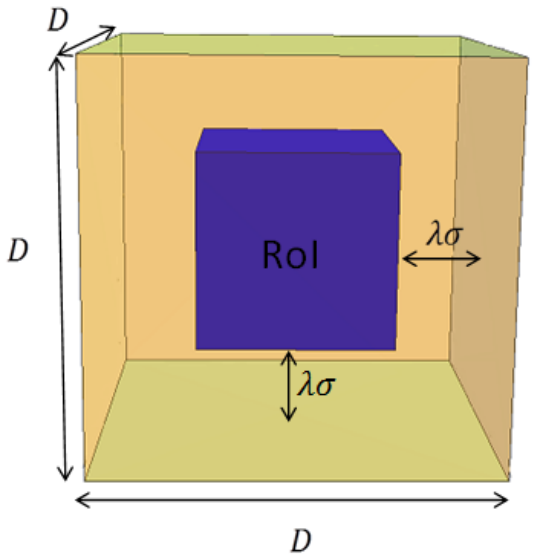

Figure 3.2: Scheme of the RoI and the original image μ.

between D and the value of λ and adjust the margins of the image so that no relevant information is removed.

3.2 Tag Pattern's Width

The Tag Pattern's width represented by L in Equation (3.1) is one of the parameters that can influence the results the most. This determines the number of tag lines that will be present in an image. In this work, a test was made to understand the relation between the number of tag lines per image, the velocity of the movement and the dimensions of the image μ.

The values for the parameters used by Equation (3.1) are in Table 3.1. Different velocities were induced to the system in the z direction.

[1]The dimension of the images used in the tests were limited by the RAM capacity of the computer in use. Therefore, the maximum value for D that was possible to analyse in a efficient time interval was 20. Nonetheless, the results where similar in a more time consuming test made for $D = 30$.

Table 3.1: Parameters used for the tag pattern's width analysis.

	Value	Unit
u	0	Pixel/Frame
v	0	Pixel/Frame
$w = w_0$	{ 0.5 , 1.5 , $\pi/2$, $\sqrt{2}$ }	Pixel/Frame
t	$[0, 19]$	Frame
L	equation (3.3)	Pixel
D[1]	20	Pixel
σ	1	Pixels
τ	1	Frames

Here L is expressed by Equation (3.3), and D is the unidirectional size of the image such that as shown in Section 3.1.

$$L \in \left[\frac{(D-5)}{D}, 2 \times D\right], \tag{3.3}$$

This means that our input image will be a 4-dimensional image with dimensions $\{x, y, z, t\} = \{20, 20, 20, 20\}$. For each value of w, an evaluation of all the values in Equation (3.3) will be made.

For a simpler comprehension of the results, the graphs "Box Whisker Chart" from *Mathematica* 9 were used in this work.

In this type of chart, the accuracy of the results is represented by the distribution boxes. Thus, if the final values are all accurate for a particular value of $\frac{L}{D}$, then the representative box will be shown as a line centered in $\frac{w_m}{w_0} = 1$. Here w_m is the value of the velocity calculated and w_0 is the value of the initial velocity given to the system. A wider box shows that there is a lower accuracy in the results. Another indicator of the accuracy are the outliers. These are values that lie outside the overall pattern of the distribution [19].

In a first evaluation of the method exact values of L were used. Meaning that for $D = 10$ and $\frac{L}{D} \in [1, 2]$ in intervals of 0.1 all the values of L would be integers from 1 to 20. Having this set of variables, only integer and half-integer values of w_0 could be

analyzed. In the following attempts, non-integer values of L were used. It was then viable to apply the method for any value of w_0. It was possible to conclude that only particular values of L can be used.

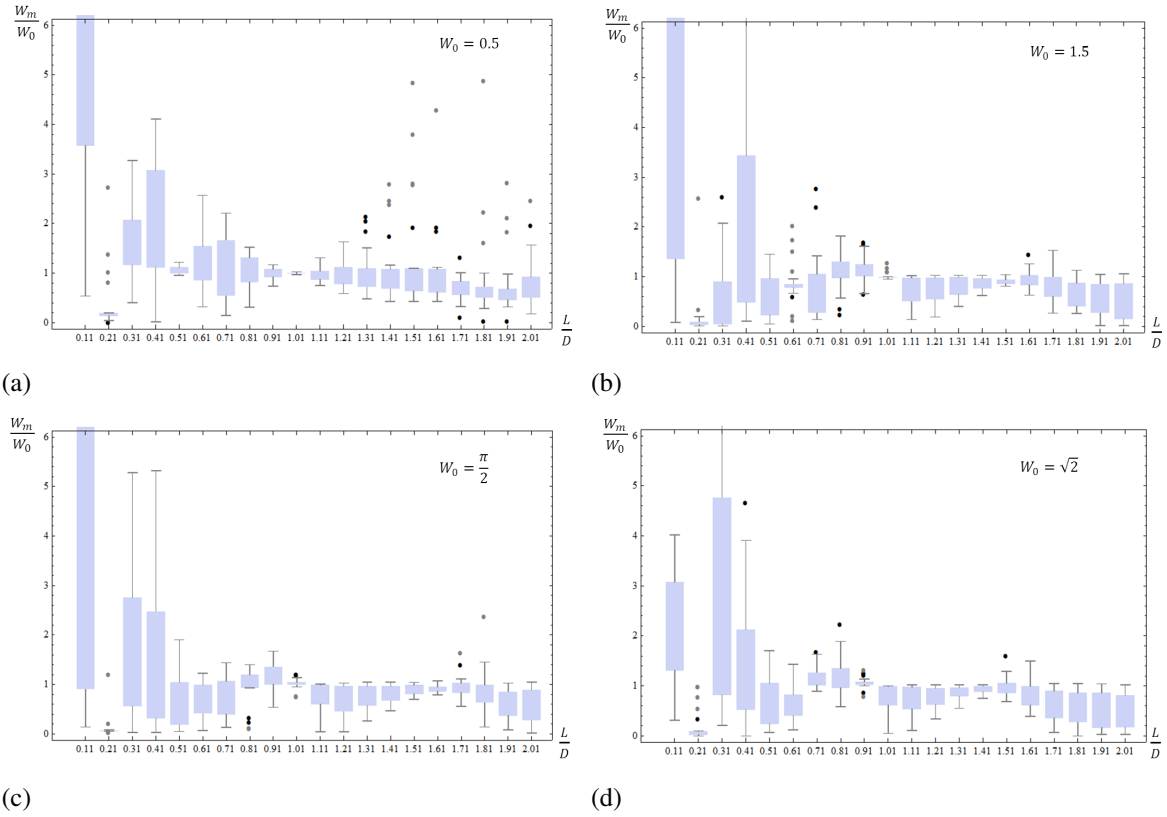

(a) (b)

(c) (d)

Figure 3.3: Tag pattern's width variation: (a) $w_0 = 0.5$; (b) $w_0 = 1.5$; (c) $w_0 = \frac{\pi}{2}$ and (d) $w_0 = \sqrt{2}\, pixels/frame$.

For $w_0 = 0.5\, pixels/frame$, it is possible to observe that the best results are obtained for $\frac{L}{D} = 0.51$ and $\frac{L}{D} = 1.01$ as presented in Figure 3.3(a). For some values of $\frac{L}{D} \leq 1.2$ there are no visible outliers. Nonetheless, in a expanded observation of the same results, it is possible to confirm that for each value of $\frac{L}{D}$ there is at least one far outlier whose value is much bigger than the value of w_0.

Setting w_0 to $1.5\ pixels/frame$ there are more than one set of acceptable results, being $\frac{L}{D} = 0.61$, $\frac{L}{D} = 1.01$ and $\frac{L}{D} = 1.51$ as it is possible to observe in Figure 3.3(b). For

$w_0 = \pi\ pixels/frame$, Figure 3.3(c), the best ratios of $\frac{L}{D}$ are in $\frac{L}{D} = 1.01$ and $\frac{L}{D} = 1.61$. Finally with $w_0 = \sqrt{2}\ pixels/frame$, in Figure3.3(d), the best values are $\frac{L}{D} = 0.91$ and $\frac{L}{D} = 1.41$.

Despite the fact that for each value of w_0 more than one acceptable value for $\frac{L}{D}$ was found, these are only applicable to a movement of specific constant velocity. Considering that the method will receive a variable velocity, it is necessary to find a common value of $\frac{L}{D}$.

By the analysis of multiple scenarios similar to the ones above, it was possible to conclude that for every value of w_0, if the size of tag pattern is close or equal to the dimension of the image, $\frac{L}{D} \approx 1.01$, the results are accurate. As a contrast, for $\frac{L}{D} = 0.21$ the values of $\frac{w_m}{w_0}$ are not acceptable.

3.3 Spatial and Temporal Scales

Another relevant factor that can affect the accuracy of the results is the scale. Following the knowledge about the OFCE method given in Section 2.2, there are two types of scales to evaluate, temporal scale τ and spatial scale σ.

Thus to solve the OFCE, 3-order Gaussian derivatives had to be used. When dealing with spatiotemporal images, space and time have their own physical scale parameter. As a result this method requires four parameters: three spatial scales σ_x, σ_y and $\sigma_z \in \Re^+$ and one $\tau \in \Re^+$ that determine the width of the Gaussians.

In terms of image representation the increase of the scale lowers the resolution such as shown in Figure 3.4. Therefore, is relevant to determine an interval for σ_x, σ_y and $\sigma_z \in \Re^+$ and $\tau \in \Re^+$ for which the assessment of the optic flow is acceptable.

Following the conclusions of the previous Section 3.2, the parameters in Table 3.2 were set for an analysis of the scales.

For the evaluation of temporal and spatial scale, multiple tests were made. In the first assessments, both values σ_z and τ were tested within $\sigma_z \in]0, 10]$ and $\tau \in]0, 10]$ separately

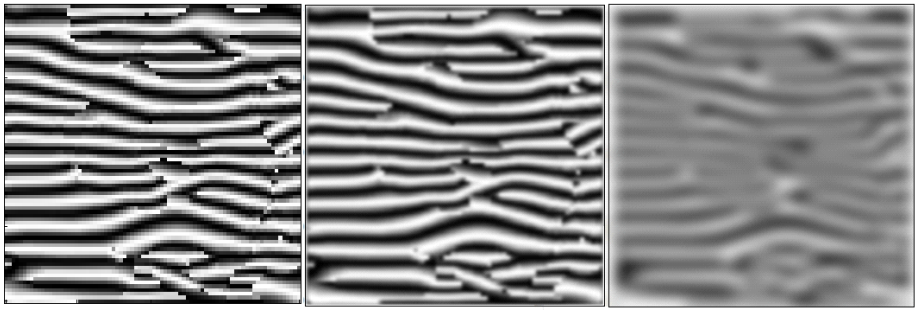

Figure 3.4: Scale space representation of Figure 2.1(c). From left to right $\sigma = 1, 4, 8 pixels$

Table 3.2: Parameters used for the scale analysis

	Value	Unit
u	0	Pixel/Frame
v	0	Pixel/Frame
$w = w_0$	{ 0.5 ,1.7, 2.4 }	Pixel/Frame
t	$[0, 19]$	Frame
L	$D + 0.1$	Pixel
D	20	Pixel

and then in simultaneous. It was possible to conclude that for smaller values of σ_z and τ the results of $\frac{w_m}{w_0}$ are better. A second group of experiments was performed. In this study the values of s and t were set to $s \in]0, 3]$ and $s \in]0, 3]$ and a study of the relation between the two variables was made.

Using the parameters in Table 3.2 multiple simulations were made and three were represented in Figure 3.5. Each representation shows the interval for the values of σ and τ that generate good results for different values of w_0. As it can be seen, there are three distinct areas represented by different colors. The red area represents the values that are not usable for being too small. The gray area represents the multiple ratios tested and the values that would be expected to work fine. Finally, the blue area contains all the values of σ and τ that generate good results.

The development of the values of the scales and the relation with the respective ratio $\frac{\sigma}{\tau}$ for $w_0 = 0.5\ pixel/frame$ can be analyzed in Figure 3.5(a). The good results of scale

are within the intervals $\sigma \in [0.63, 3.2]\ pixels$ and $\tau \in [0.63, 2]\ frames$. Nonetheless, these values are restricted to appear in a certain ratio. Having a maximum ratio of 3 $pixels/frame$ for $\tau = 0.63\ frames$ and a minimum $\frac{\sigma}{\tau} = 1.7\ pixels/frame$ for $\tau = 2$ $frames$.

Taking now in consideration $w_0 = 1.7\ pixel/frame$, shown in Figure 3.5(b), the blue area is restricted to the intervals $\sigma \in [0.63, 3]\ pixels$ and $\tau \in [0.63, 2]\ frames$. The minimum ratio is $3\ pixels/frame$ and the maximum value for $\frac{\sigma}{\tau}$ is $1.5\ pixels/frame$. At last for $w_0 = 2.4\ pixel/frame$, in Figure 3.5(c), the interval for spatial and temporal scales are $\sigma \in [0.63, 3]\ pixels$ and $\tau \in [0.63, 2]\ frames$, and the maximum and minimum values for $\frac{\sigma}{\tau}$ are 3 and $1.2\ pixels/frame$ respectively.

A smooth decline of the ratios $\frac{\sigma}{\tau}$ with the increase of the value of τ and w_0 can be seen in Figure 3.5.

The relative error δ was calculated for each value of σ above the acceptable ratio of $\frac{\sigma}{\tau}$. These are presented as different colored dots (Magenta, Red and Black) representing $\delta < 20\%$, $\delta < 40\%$ and $\delta > 40\%$ respectively. For every value of w_0 it is possible to detect a growth in the errors above the maximum acceptable ratio. Likewise, the increase of the relative error δ is sharper for larger values of w_0.

In a situation where the input velocity is unknown the safest interval of ratios to use is the one below the minimum value of $\frac{\sigma}{\tau}$ obtained in the study, this being $1.2\ pixels/frame$. In tests made with larger values of D the results obtained were similar. Therefore, we can conclude that the best values of σ and τ to use are $\sigma \in [0.63, 3.2]\ pixels$ and $\tau \in [0.63, 2]$ $frames$ and with $\frac{\sigma}{\tau} \leq 1\ pixels/frame$.

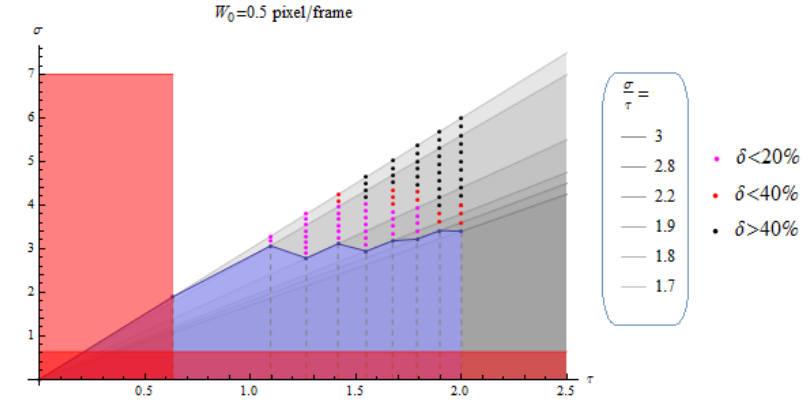

(a)

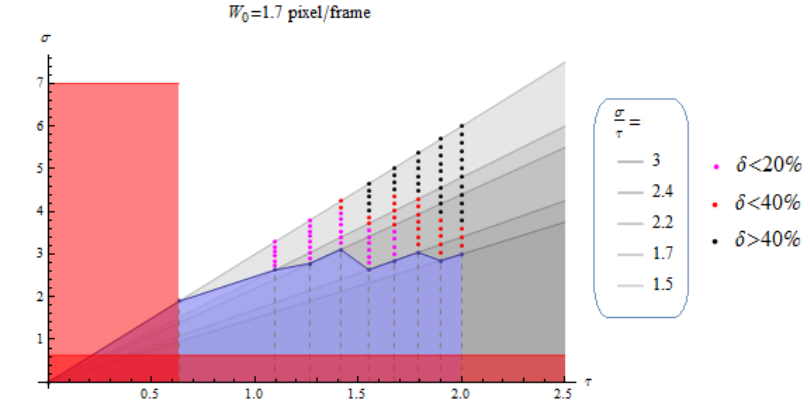

(b)

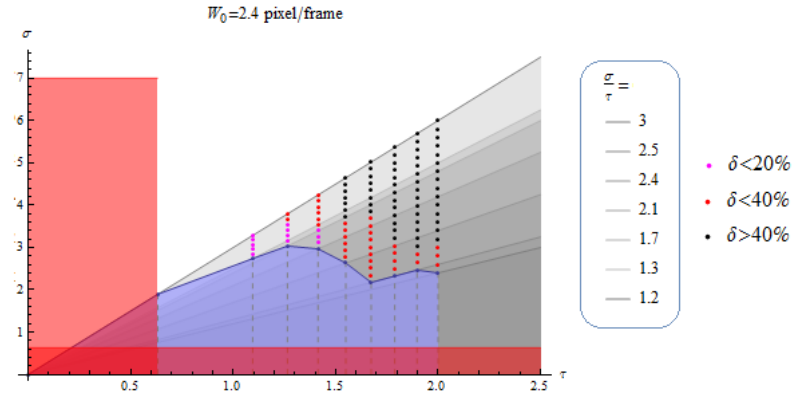

(c)

Figure 3.5: Interval for spatial and temporal scale for: (a) $w_0 = 0.5\ pixel/frame$, (b) $w_0 = 1.7\ pixel/frame$, (c) $w_0 = 2.4\ pixel/frame$.

Chapter 4

The Influence of Noise

So far we have simulated and analyzed the effect of a variety of factors that can influence the results obtained by OFCE. Nevertheless this has been made with simple examples of sinusoidal functions like Equation (3.1). With the goal of mimicking as closely as possible, the input given by a tagged MR image, it is necessary to consider the influence of noise.

When talking about image processing, noise is a common problem. Consequently, one of the first steps required to retrieve and analyse relevant information from a image is denoising. Despite the extensive literature existent about this process, it is imperative that we know what type of noise we are dealing with. Commonly, the assumption that the noise in MR images is defined by Gaussian distribution is made. This would simplify the method of deblurring and filtering, but generates poor quality results. In 1984, Edelstein et al. [20] proved that noise in magnitude MR images is governed by the Rayleigh distribution, later in 1989 Bernstein et al. [21] presented a closed form solution of the more general Rician distribution. It is then, in 1995, that Gudbjartsson et al. [22] presents a way to express noise with a Rician distribution for both magnitude and phase MR images.

As explained in Section 2.1 the input images for the OFCE method are phase images. These are obtained after the use of the HARP method and the application of the Sine function as shown in Figure 2.1. According to Ding et al. [23] a sinusoidal function mixed

with noise can be expressed by Equation (4.1).

$$y(t) = \mu(t) + n(t) \tag{4.1}$$

Where $y(t)$ is the noisy image, $\mu(t)$ is the clean image generated in Chapter 3 (Equation (3.1)) and $n(t)$ the noise. Following the statements made before in this section, $n(t)$ will be defined as a Rician distribution, also known as Rice density or Rice distribution. Therefore, the distribution of the phase noise Δ_θ is given by Equation (4.2).

$$P_{\Delta_\theta} = \frac{1}{2\pi} e^{-A^2/2\sigma^2} \left[1 + \frac{A}{\sigma}\sqrt{2\pi}\cos\Delta_\theta e^{A^2\cos^2\Delta_\theta/2\sigma^2} \cdot \frac{1}{2\sqrt{\pi}} \int_{-\infty}^{\frac{A\cos\Delta_\theta}{\sigma}} e^{-\chi^2/2} d\chi \right] \tag{4.2}$$

Where A is the image pixel intensity without noise. Despite the complexity of Equation (4.2), when $A \gg \sigma$ the distribution can be considered as a zero mean Gaussian distribution [22]. Also when $\frac{A}{\sigma} = 0$ a Rayleigh distribution is obtained [23].

Having that, it is possible to reanalyze all the factors tested in Chapter 3 with the influence of noise.

With the addition of noise, not only the pixel intensity of the input image will change, but also the variables necessary to assess the viability of the method. For a better understanding of the results presented in the following section, these will be continuously confronted with Chapter 3. Therefore, the conditions tested will be similar.

Regarding the boundaries effect, there was no evident influence of noise in the artifacts. For this reason all the tests regarding the noise influence will use the parameters of the RoI as explained in Section 3.1.

4.1 Tag Pattern's Width

In Section 3.2, it was concluded that the suitable values of $\frac{L}{D}$ are approximately one and that only non-integer values of L can be used. Using the conditions presented in Table 4.1 it was possible to assess the effect of the Rician noise.

Table 4.1: Parameters used for the Tag Pattern's Width analysis with the addition of Rician noise

	Value	Unit
u	0	Pixel/Frame
v	0	Pixel/Frame
$w = w_0$	{ 0.5 , 1.5 , $\pi/2$, $\sqrt{2}$ }	Pixel/Frame
t	$[0, 19]$	Frame
L	Equation (3.3)	Pixel
D[1]	20	Pixel
σ	2	Pixels
τ	2	Frames

While in tests made without noise the best solutions were found in $\frac{L}{D} \in [0, 2]$, after the addition of noise this was no longer a suitable interval. As we can see in Figure 4.1, the values below $\frac{L}{D} = 1.01$ are much smaller than $\frac{w_m}{w_0} = 1$ and therefore unacceptable. Hence it was used a new interval for the evaluation of the width of tag patterns.

The best solutions were then found in the interval $\frac{L}{D} \in [1, 3]$. For the velocity $w_0 = 0.5$ $pixels/frame$ in Figure 4.2(a), $\frac{L}{D} = 2.01$ is the best result possible. There is a bigger occurrence of outliers for values above the optimal result. Also, it is notable the decrease in the accuracy of $\frac{w_m}{w_0}$ as $\frac{L}{D}$ deviates from $\frac{L}{D} = 2.01$. Such as the previous analysis, also for $w_0 = 1.5\, pixels/frame$, in Figure 4.2(b), the best result found was for $\frac{L}{D} = 2.01$. The decrease of accuracy for the results as $\frac{L}{D}$ deviates from the optimal value is also notable. There is a strong decline of the accuracy for the values of $\frac{w_m}{w_0}$ as $\frac{L}{D}$ decreases.

Considering now $w_0 = frac\pi 2\ pixels/frame$, in Figure 4.2(c), there is only one occurrence of $\frac{L}{D}$ for which the value of $\frac{w_m}{w_0}$ is acceptable, $\frac{L}{D} = 2.11$. Finally for $w_0 = \sqrt{2}$ $pixels/frame$, in Figure 4.2(d), there is no optimal result. Nonetheless, the results in

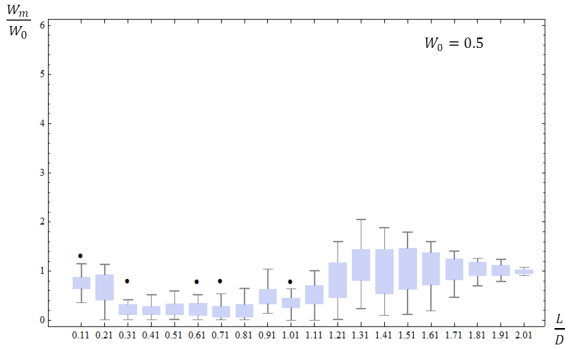

Figure 4.1: Tag pattern's width variation from 0 to 2 with influence of Rician noise:$w_0 = 0.5\, pixels/frame$.

$\frac{L}{D} \in [1.81, 2.01]$ and $\frac{L}{D} \in [2.61, 2.71]$ are considered acceptable.

Analyzing all the results as a group, in Figure 4.2, there is a constant decline of the accuracy of $\frac{w_m}{w_0}$ for $\frac{L}{D} \leq 1.81$. It is also possible to observe that regardless of the values of $\frac{w_m}{w_0}$ are very close to one for $\frac{L}{D} \geq 2.11$, these tend to have a bigger distribution as $\frac{L}{D}$ increases. The best results were mostly found in values of $\frac{L}{D}$ approximated to 2.

4.1.1 Quantity of Noise

Later experiments where made to evaluate the influence of the quantity of the noise in the results. In the previous tests made in Section 4.1 a random function was used to generate the Rician noise $n(t)$ (Equation (4.1)). The manipulation of the interval of the random generation allowed to simulate a wider concentration of noise and also a more narrow concentration.

It was possible to conclude that there are differences in the results with a small quantity of noise and with a lot of noise, shown in Figure 4.3. Just as expected, for tag pattern's width below D and with $n(t) \in [1, 10]$, presented in Figure 4.3(b), the results obtained were worse than with $n(t) \in [0, 0.3]$, as is possible to observe Figure 4.3(a). Nonetheless, the results obtained are not distinct enough and the conclusions remain the same as the ones of previous analysis.

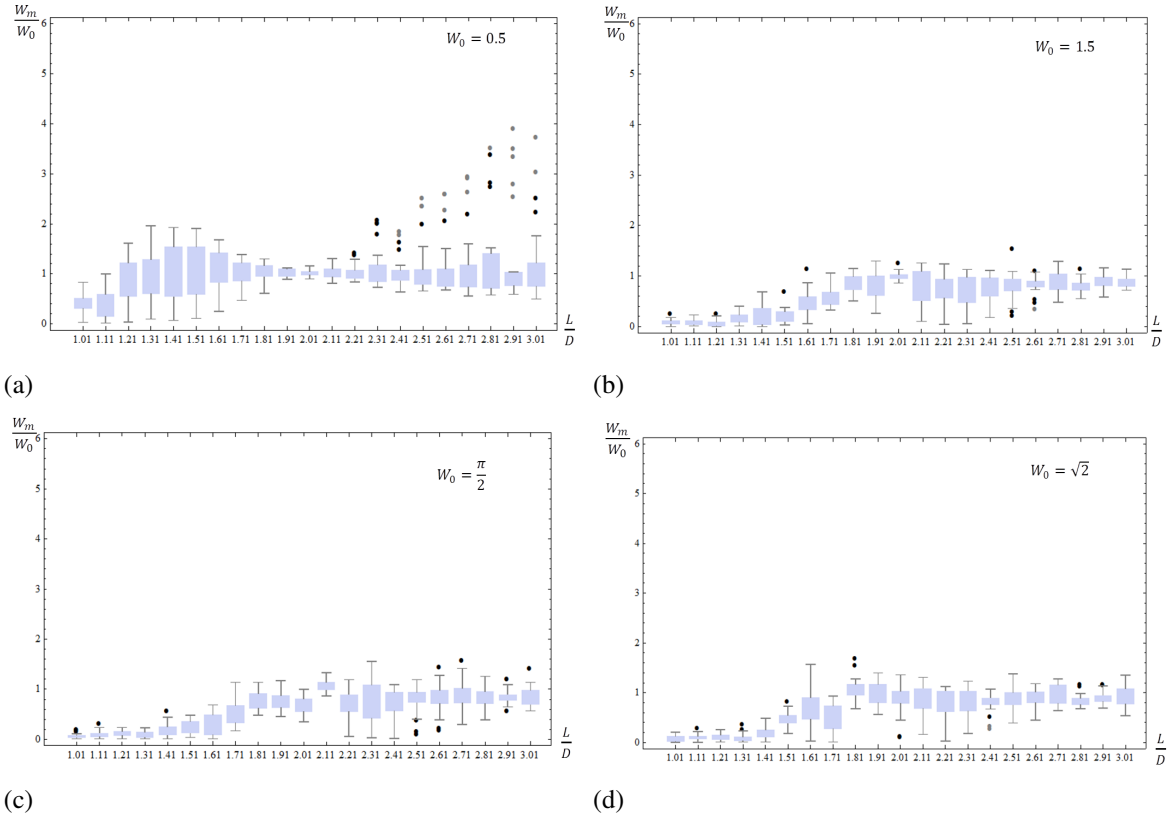

Figure 4.2: Tag pattern's width variation from 1 to 3 with influence of Rician noise: (a) $w_0 = 0.5$; (b) $w_0 = 1.5$; (c) $w_0 = \frac{\pi}{2}$ and (d) $w_0 = \sqrt{2}\, pixels/frame$.

Ended the evaluation of the tag pattern widths with the addition of Rician distributed noise, we can conclude that the best tag pattern width to use should be a non-integer number and approximately the double of the dimension D of the image.

4.2 Spatial and Temporal Scales

As it was possible to see in the previous sections, there are evident differences in the results obtained with a clean image and with noisy images.

Thus following the conclusions taken in Section 4.1, the influence of noise in spatial

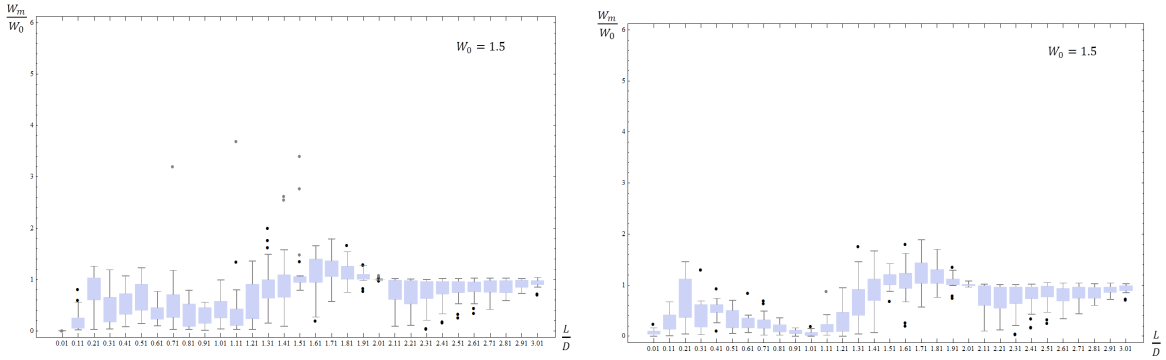

(a) (b)

Figure 4.3: Noise quantity variation for a $w_0 = 1.5\, pixel/frame$. Results with (a) $n(t) \in [0, 0.3]$; (b) $n(t) \in [1, 10]$

and temporal scales was evaluated with the parameters presented in Table 4.2. The values of σ and τ are explained in Section 3.3.

Table 4.2: Parameters used for the Scale analysis with rician noise

	Value	Unit
u	0	Pixel/Frame
v	0	Pixel/Frame
$w = w_0$	{ 0.5 ,1.7, 2.4 }	Pixel/Frame
t	$[0, 19]$	Frame
L	$2D + 0.1$	Pixel
D	20	Pixel

After extensive testing it was possible to conclude that there are relevant differences regarding the spatial and temporal scales to be used with noise. For smaller values of w_0 like $w_0 = 0.5\, pixels/frame$ the maximum value for $\frac{\sigma}{\tau}$ was $2.5\, pixels/frame$ and it was found for $\tau = 0.63\ frames$. There is a strong decline of $\frac{\sigma}{\tau}$ with the increase of τ where the maximum value of τ acceptable is $\tau = 2\ frames$. Also, for the values above the acceptable ratios, there is a strong increase in the relative error, δ with the increase of σ, such as is possible to observe in Figure 4.4(a).

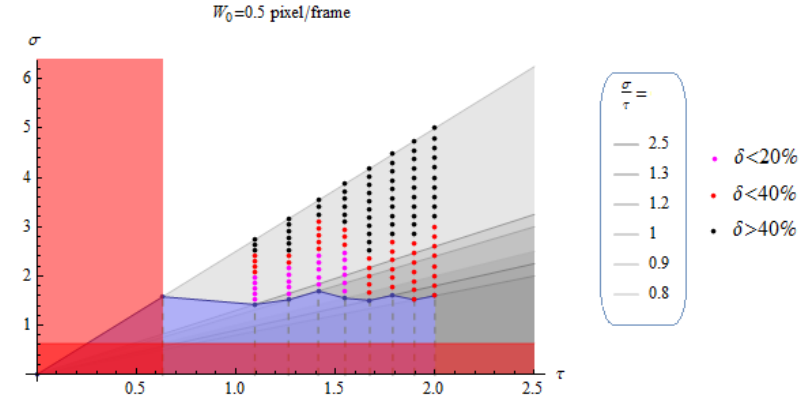

(a)

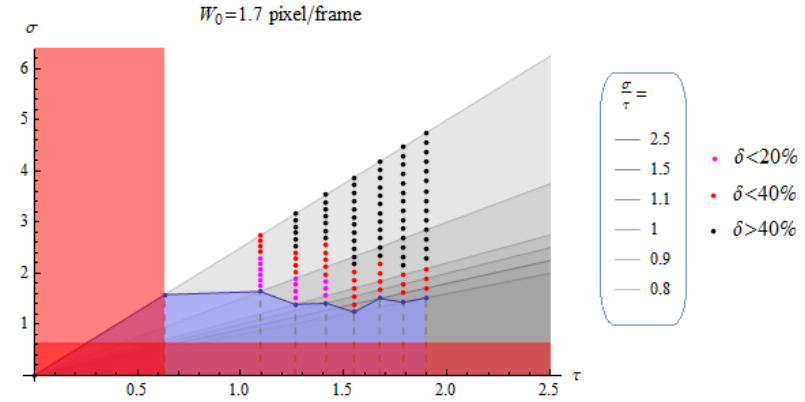

(b)

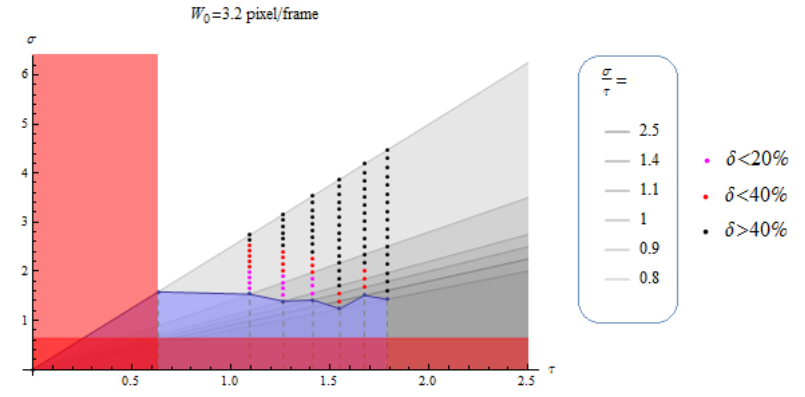

(c)

Figure 4.4: Interval for spatial and temporal scale for: (a) $w_0 = 0.5\ pixel/frame$, (b) $w_0 = 1.7\ pixel/frame$, (c) $w_0 = 3.2\ pixel/frame$.

Analyzing the results for $w_0 = 1.7\, pixels/frame$, we can find a similar evolution as in $w_0 = 0.5\, pixels/frame$. The main difference between the two velocities is the maximum value of τ. Likewise, the decline of $\frac{\sigma}{\tau}$ is sharper than in $w_0 = 0.5\, pixels/frame$. This can be easily observed by comparing Figure 4.4(a) and 4.4(b).

For the value of $w_0 = 3.2\, pixels/frame$, the results obtained were more restricted than for smaller values w_0. For this velocity the maximum value of τ that is capable of generating results with an error below $\delta < 10\%$ is $\tau = 1.8\ frames$ for which the maximum value of $\frac{\sigma}{\tau}$ is $0.8\, pixels/frame$ as shown in Figure 4.4(c).

Despite the fact that the minimum values of σ and τ remain the same for each value of w_0, there is an evident relation between the maximum temporal scale τ acceptable and the input velocity w_0. Nonetheless, it is still possible to establish a safe interval for σ, τ and the ratio $\frac{\sigma}{\tau}$ were the results generated are acceptable for any value of w_0. They are

$$\sigma \in [0.63, 1.38]\, pixels$$
$$\tau \in [0.63, 1.26]\ frames$$
$$\tfrac{\sigma}{\tau} \in [0, 1.1]\, pixels/frame.$$

4.3 Dimension D

During the evaluation of the scales in Section 4.2 it was found a strong relation between the dimension D of the image and the input velocities w_0. During the tests made with $D = 10\, pixels$, the input velocities for which the method was capable to produce results with errors $\delta < 10\%$ were $w_0 < 2.5\, pixel/frame$. Therefore, when produced a graph for $w_0 = 2.4\, pixel/frame$, this presents a very restrict interval of σ and τ, such as in Figure 4.5.

In order to understand if the case presented was a isolated phenomena the analysis of the relation $\frac{w_0}{D}$ was made for bigger values of D. The result was a constant pattern for every value of D. Once the value of w_0 approximates to one forth of D, the value of the ratio $\frac{w_0}{w_m}$ declines and the accuracy of the results decreases with the increase of w_0. The

effect can be synthesized by Figure 4.6.

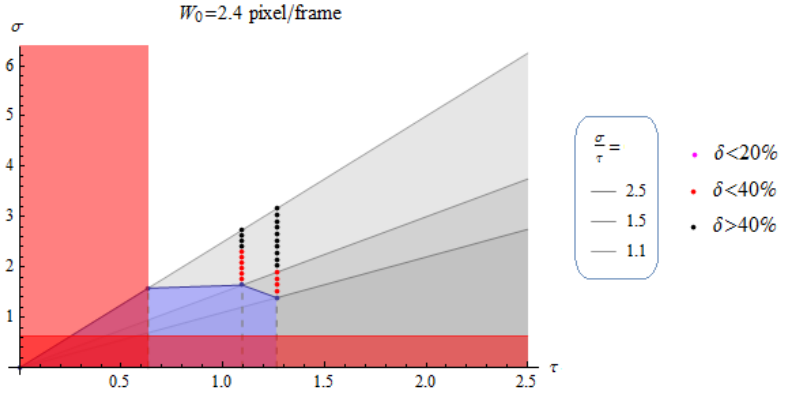

Figure 4.5: Scales evaluation graph for $w_0 = 2.4\ pixels/frame$ and $D = 10\ pixels$.

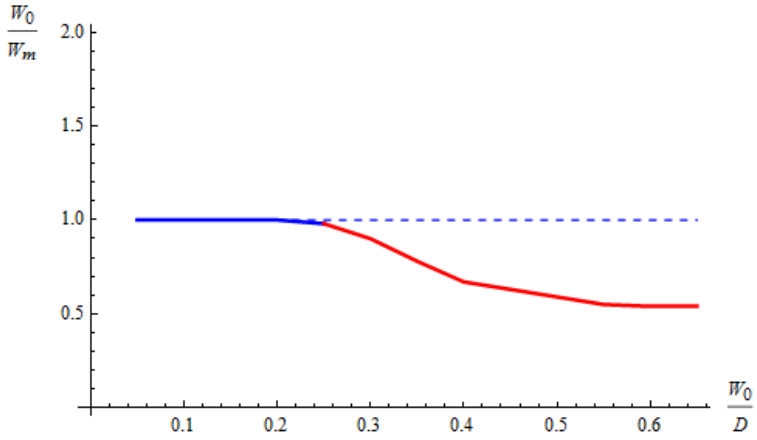

Figure 4.6: Relation $\frac{w_0}{D}$ in noisy images.

Ideally, there would be no relation between dimension and the velocities. Nonetheless, as exposed in Section 3.1 is possible to manipulate the dimension of the image D in order to get the best possible results. Considering that the real velocities of the myocardium are within $[1.846, 3.07]\ pixel/frame$, as shown in Section 2.3, the dimension D should be at least four times bigger than the maximum w_0 (w_{0max}). The recommended value of D would then be $D > 4 \times w_{0max}$ i.e. $D > 12\ pixels$.

Chapter 5

Conclusion

The main goal of this dissertation project was to present the limitations and constrains of the OFCE regarding the quantification of myocardial movement using tagging MR images. Initially, it was also stipulated that if the method would be proven efficient, having time and disposability resources, this would be combined with a Cardiac Motion Simulator to detect abnormalities in the motion of the heart.

By the end of the project multiple scenarios were simulated and tested in order to asses the constrains of the OFCE method when applied to tagging MR images. It was then possible to assemble a group of factors that can affect the accuracy of the results and the best way to optimize the method was discussed. This discussion contemplates multiple situations including synthetic tagged MR images with and without Rician noise.

With this study it was possible to unravel very important characteristics of the OFCE method and the tagged MR images. In the evaluation of the method with clean synthetic images it was discovered a relation between the boundaries artifacts and the accuracy of the method. Also the tag pattern as an important influence in the method such as the temporal and spatial scales. Following tests made with noisy images, proved that the same factors still affect the results but in a different way. During this survey it was found that the dimension of the images can also affect the results. For the expected values of the movement of the myocardium of $[1.846, 3.07]\ pixel/frame$, it was determined a interval

of values for which the velocities would be achieved with minimal errors.

During the development of this work many difficulties were found. The first stage of the project included the familiarity with a new software which revealed to be a extensive time consuming task. Not all the goals settled in the beginning of the project were concluded due to the discovery of a wide group of limitations of the method. In order to provide the reader to the most accurate results an extensive series of tests were made simulating every case possible. Unfortunately, due to the RAM limitations of the computers provided, this was a task that consumed the majority of the time of the project.

5.1 Future Work

In a future work, the first step would be to complete the evaluation of the factors with a study of the outliers. The Outliers revealed a certain pattern during the tests, so the theory that these might be connected with the borders of the tag patterns would be worth considering.

After an extensive testing series to prove that the outliers are indeed a relevant variable it would be possible to complete the goals of this project with the combination of the OFCE with the CMS.

Finally, this prototype together with some acquired knowledge about heart malfunctions, would allow the construction of a application capable to detect and diagnose heart diseases.

Such as mentioned in the previous paragraphs not all the goals were achieved. Nonetheless, the knowledge obtained is fundamental to understand up to what extend the OFCE is a valid method for the detection of Optic Flow in tagged MR images. Despite all the restrictions and limitation, the OFCE shows a great potential for the detection and quantification of Optic Flow using tagged MR images. With the correct manipulation, this method can be used to create new applications that can improve medical care.

Appendix A

Cardiac Motion Simulator

Like any other method created with the goal of evaluating a specific behavior it is fundamental to be able to recognize and distinguish a normal event from defective occurrences. In the specific case of the method described in this work it is necessary to establish ground truth for myocardial deformation, strain and movement velocities. The evaluation of these variables revealed to be possible with the use of an adaptation of the cardiac motion simulator (CMS) for tagged MR, developed by Waks et al. [1]. The CMS developed by Waks et al. [1] incorporates a 13-parameter model of left ventricular motion applied to a confocal prolate spherical shell, which resembles the shape of the left ventricle (LV). Using the CMS, true motion can be computed in two or three dimensions and used as a comparative reference for motion estimation algorithms. Therefore, it is imperative to ensure that the simulations are representative of a true cardiac motion.

The CMS developed within the context of this work is a simplified version of Waks' et al. [1] model that uses only 10-parameters, discarding translational factors. Using the CMS is then possible to obtain strain and deformation as well as to create synthetic tagged MR images.

A.1 Cardiac Motion Simulator

A.1.1 Shape

The model developed by Waks et al. [1] is based on data obtained by Arts et al. [3] as a result of a bead experiment on a dog heart. The basis of the geometric model is the prolate sphere, which is a three-dimensional ellipsoidal object. A point in the prolate sphere is defined by (λ, η, ϕ) where λ is the radius, η the elevation angle and ϕ the azimuthal angle. These variables can also be expressed in Cartesian coordinates as shown in Equation (A.1)

$$\begin{aligned} x &= \delta \sin h \;\; \lambda \sin \eta \cos \phi \\ y &= \delta \sin h \;\; \lambda \sin \eta \sin \phi \\ z &= \delta \cos h \;\; \lambda \cos \eta \end{aligned} \tag{A.1}$$

Here δ is a fixed parameter called the focal radius (the distance from the origin to either focus). In order to define a point (x, y, z) in prolate spheroidal coordinates, one can use Equations (A.2)

$$\begin{aligned} \lambda &= \cos h^{-1} \frac{r_1 + r_2}{2\delta} && (\lambda > 0), \\ \eta &= \cos^{-1} \frac{r_1 - r_2}{2\delta} && (0 \leqslant \eta \leqslant 180), \\ \phi &= \tan^{-1} \frac{y}{x} && (0 \leqslant \phi \leqslant 360), \\ r_1 &= \sqrt{x^2 + y^2 + (z+\delta)^2} \\ r_2 &= \sqrt{x^2 + y^2 + (z-\delta)^2} \end{aligned} \tag{A.2}$$

The LV can be defined by λ_0 and λ_i, where λ_0 is the outer radius and λ_i the inner radius of the myocardium with $\lambda_i < \lambda_0$. Given the restriction $0 \leqslant \eta \leqslant 120$ and using the values specified in Table A.1, it is possible to build the model of the LV shown in Figure

A.1 with the prolate sphere.

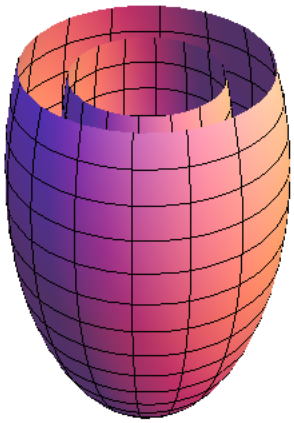

Figure A.1: Example of a LV's inner and outer layers using the CMS model. Settings as in Table A.1.

Table A.1: Constant values model.

Constant	Description	Value	Unit
λ_i	Inner radius	0.35	None
λ_0	Outer radius	0.55	None
δ	Focal radius	4.00	cm

A.1.2 Motion

As mentioned before the model of Arts et al. [3] induces deformation based on the 13 parameters k_1 to k_{13} listed in the Table A.2. However the simplified model discards the translational factors meaning that the parameters k_{11} to k_{13} are set to zero.

Motion is specified by a transformation which maps a material point $\mathbf{p}$ to a corresponding spatial point $\mathbf{r}$ at a time t. When the LV deforms, the spatial coordinates corresponding to the material points change. To obtain the final matrix that transforms point $\mathbf{p} = (p_x, p_y, p_z)$ into $\mathbf{r}(t) = (r_x, r_y, r_z)$ several matrices where defined in [1], namely $\mathbf{F}_0$

trough $\mathbf{F}_6$ and $\mathbf{F}_b$ described in Appendix A.5. The overall equation for transforming point **p** to point **r** is Equation (A.3)

$$\mathbf{r} = \mathbf{F}_b\mathbf{F}_6\mathbf{F}_5\mathbf{F}_4\mathbf{F}_3\mathbf{F}_2\mathbf{F}_1\mathbf{F}_0\mathbf{p} \tag{A.3}$$

For each step in time it is necessary to compute the value of all ten k-parameters. Arts et al. [3] used the Levenberg-Marquardt parameter estimation algorithm to estimate all ten parameters. In order to simulate all the parameters between end-diastole and end-systole, simplified equations have been used, see Equations (A.4) given below. The parameters can be obtained according to Equation (A.3).

$$\begin{aligned}
k_1 &= \frac{(t-8)^2}{320} - 0.1 \\
k_2 &= \frac{-(t-8)^2}{320} + 0.1 \\
k_3 &= \frac{-(t-8)^2}{640} + 0.04 \\
k_4 &= -0.03 \\
k_5 &= 0.001875t - 0.02 \\
k_6 &= 0.00046875t^2 - 0.0075t \\
k_7 &= 0.00234375t^2 - 0.0375t + 0.06 \\
k_8 &= -0.00375t + 0.03 \\
k_9 &= 0.08 \\
k_{10} &= -0.001875t - 0.22
\end{aligned} \tag{A.4}$$

The overall equation for transforming material point **p** to spatial point **r** is given by Equation (A.3). If **A** is a transformation matrix determined by matrices $\mathbf{F}_0$ through $\mathbf{F}_6$ and

$\mathbf{F}_b$ then Equation (A.3) can be rewritten in the simplified way

$$\mathbf{r} = \mathbf{A}\mathbf{p} \tag{A.5}$$

All the k-parameters depend on a time instant and are modeled according to the results of Waks et al. [1]. Spatial points **r** are determined for each time frame from the material points **p**, which means no preceding time frames are required to determine the next.

Arts et. al [3] developed a method to produce deformation using 13 k-parameters. The main goal is to compute strain and deformation, therefore the parameters k_{11} to k_{13} regarding translation don't bring any relevant information and so these are set to zero. The description of the original 13 k-parameters is presented in Table A.2.

Table A.2: Parameters for the motion model based in Arts et al. [3] deformation theory.

k_1	Radially dependent compression
k_2	Left ventricular torsion
k_3	Ellipticallization in long axis planes
k_4	Ellipticallization in short axis planes
k_5	Shear in z direction
k_6	Shear in y direction
k_7	Shear in x direction
k_8	Rotation about x-axis
k_9	Rotation about y-axis
k_{10}	Rotation about z-axis
k_{11}	Translation in x direction
k_{12}	Translation in x direction
k_{13}	Translation in x direction

A.2 Synthetic Tagged MR Images

In order to use ground truth motion, synthetic tagged MR images also need to be created. If the model is validated, the images can be used to evaluate the OFCE method. Realistic tag patterns are generated by using a tagged MR imaging equation as described

in Prince et al. [24]. The pixel intensity value for each point **r** is μ, which is given by

$$\mu = D_0 e^{\frac{-T_E}{T_2}} \times \left(1 + ((1 - e^{-T_R - t_d})\xi(\mathbf{r}) - 1)e^{\frac{-t_d}{T_1}}\right) \tag{A.6}$$

Where, $t_d = t_i - t_0$ and D_0, T_1 and T_2 are constants representing spin density, longitudinal relaxation time and transverse relaxation time respectively. These constants are determined by the properties of the LV. T_E and T_R are the echo and pulse repetition time. All these parameters have to be specified, see Table A.3. The function $\xi(\mathbf{r})$ represents the tag pattern and is given by

$$\begin{aligned} \xi(\mathbf{r}) =& (\cos^2\theta - \sin^2\theta \cos k_x r_x) \times \\ & (\cos^2\theta - \sin^2\theta \cos k_y r_y) \times \\ & (\cos^2\theta - \sin^2\theta \cos k_z r_z) \end{aligned} \tag{A.7}$$

k_x, k_y and k_z are spatial frequencies in the x, y and z directions respectively. θ is the tag pattern flip angle, which is the angle by which longitudinal magnetization is tipped towards the transverse plane (there is an overall increase in brightness as the flip angle increases) [25]. Prince et al. [24] only provide $\xi(\mathbf{r})$ in the x and y direction, whereas Equation (A.7) has been extended in the z direction. In order to obtain images with tagging lines in e.g. the x direction, one has to set k_y and k_z to zero, and similarly for lines in the other directions.

To create images from the transformed data, interpolation needs to be done since the points **r** are no longer on a regular grid in the Cartesian coordinate system. A weighted linear interpolation is used, for which the three nearest neighbors are taken into account.

Table A.3: Constants tagged spin-echo MR imaging equation.

	Description	Value	Unit
D_0	Spin density	300	None
T_E	Echo time	0.03	Sec
T_R	Pulse repetition time	10	Sec
T_1	Spin-lattice relaxation time	0.6	Sec
T_2	Spin-spin relaxation time	0.1	Sec
k_x	Frequency in x	8.0/0.0	rad/cm
k_y	Frequency in y	8.0/0.0	rad/cm
k_z	Frequency in z	8.0/0.0	rad/cm
θ	Tip angle of tag pattern	45.00	Degrees

A.3 Deformation

To obtain the Green-Lagrange strain tensor **E**, the deformation gradient tensor **F** is required. The matrices representing torsion and ellipticallization depend on the material points **p**, see Appendix A.5, Equations (A.12) to (A.15). Therefore to obtain the deformation gradient tensor F, the derivation in Equation (A.8) is required.

$$F_{ij}(\mathbf{p}) = \frac{\partial \mathbf{r}_i(\mathbf{p})}{\partial \mathbf{p}_j} = \sum_{k=1}^{3} \frac{\partial A_{ik}(\mathbf{p})}{\partial \mathbf{p}_j} \mathbf{p}_k + A_{ij}(\mathbf{p}), \tag{A.8}$$

(A.9)

Here $i, j = 1, 2, 3$.

Equation (A.8) shows that the derivative of the new coordinates **r** with respect to the old coordinates **p** has to be obtained. The deformation gradient tensor **F** is only equal to transformation matrix A, when the latter does not depend on material points **p**.

A.4 Strain

Once the deformation gradient tensor **F** is computed we can calculate the Green-Lagrange strain tensor **E**, defined by Equation (A.10).

$$E_{ij} = \frac{1}{2}(F_{ki}F_{kj} - \delta_{ij}) \tag{A.10}$$

Considering that $i, j, k = 1, 2, 3$ we have the Equation (A.11)

$$\mathbf{E} = \frac{1}{2}(\mathbf{F}^T\mathbf{F} - \mathbf{I}) \tag{A.11}$$

Here I is the identity matrix and δ_{ij} is the Kronecker delta ($\delta_{ij} = 1$ if $i = j$ and 0 otherwise).

In order to investigate the properties of **E**, the eigenvalues, determinant and trace are calculated. Also, the Frobenius norm of a diagonal matrix containing the eigenvalues of **E** in arbitrary order (i.e. the sum of the squared eigenvalues) is computed.

A.5 Matrices developed by Waks et al.[1]

In order to resolve Equation A.3 proposed by Waks et al.[1] is necessary to compute the matrices $\mathbf{F}_0$ to $\mathbf{F}_6$ and $\mathbf{F}_b$. The matrices (A.12) to (A.18) give us all the elements necessary to compute the **F**- matrices.

$$\mathbf{F}_0 = \begin{bmatrix} a^{\frac{1}{3}} & 0 & 0 \\ 0 & a^{\frac{1}{3}} & 0 \\ 0 & 0 & a^{-\frac{2}{3}} \end{bmatrix} \tag{A.12}$$

$$\mathbf{F}_1 = \begin{bmatrix} \epsilon & 0 & 0 \\ 0 & \epsilon & 0 \\ 0 & 0 & \epsilon \end{bmatrix}, \qquad \epsilon = \sqrt[3]{1 + \frac{3k_1V_w}{4\pi|F_0\mathbf{p}|^3}} \tag{A.13}$$

$$\mathbf{F}_2 = \begin{bmatrix} \frac{\cos ak_2 z_1}{|r_1|} & \frac{-\sin ak_2 z_1}{|r_1|} & 0 \\ \frac{\sin ak_2 z_1}{|r_1|} & \frac{\cos ak_2 z_1}{|r_1|} & 0 \\ 0 & 0 & 1 \end{bmatrix}, \tag{A.14}$$

$$\mathbf{r}_1 = \mathbf{F}_1\mathbf{F}_0\mathbf{p} = \begin{bmatrix} x_1 \\ y_1 \\ z_1 \end{bmatrix}$$

$$\mathbf{F}_3 = \begin{bmatrix} a^{-\frac{1}{3}}e^{k_4-(\frac{k_3}{2})} & 0 & 0 \\ 0 & a^{-\frac{1}{3}}e^{-k_4-(\frac{k_3}{2})} & 0 \\ 0 & 0 & a^{\frac{2}{3}}e^{k_3} \end{bmatrix} \tag{A.15}$$

$$\mathbf{F}_4 = \begin{bmatrix} 1 & k_5 & 0 \\ k_5 & 1+{k_5}^2 & 0 \\ 0 & 0 & 1 \end{bmatrix}$$

$$\mathbf{F}_5 = \begin{bmatrix} 1 & 0 & k_6 \\ 0 & 1 & 0 \\ k_6 & 0 & 1+{k_6}^2 \end{bmatrix} \tag{A.16}$$

$$\mathbf{F}_6 = \begin{bmatrix} 1 & 0 & 0 \\ 0 & 1 & k_7 \\ 0 & k_7 & 1+{k_7}^2 \end{bmatrix} \tag{A.17}$$

$$\mathbf{F}_b = \mathbf{B}_3\mathbf{B}_2\mathbf{B}_1,$$

$$\mathbf{B}_1 = \begin{bmatrix} 1 & 0 & 0 \\ 0 & \cos k_8 & -\sin k_8 \\ 0 & \sin k_8 & \cos k_8 \end{bmatrix}$$
$$\mathbf{B}_2 = \begin{bmatrix} \cos k_9 & 0 & \cos k_9 \\ 1 & 0 & 1 \\ -\sin k_9 & 0 & \cos k_9 \end{bmatrix} \tag{A.18}$$
$$\mathbf{B}_3 = \begin{bmatrix} \cos k_{10} & -\sin k_{10} & 0 \\ \sin k_{10} & \cos k_{10} & 0 \\ 0 & 0 & 1 \end{bmatrix}$$

In the Equations (A.12), (A.13), (A.14) and (A.15) Waks et al.[1] uses two extra parameters a and V_w. Parameter a is used for correction in matrix F_0, which transforms a prolate sphere into a more spherical shape, to deal with possible uniform distortion by compression, see Equation (A.19). After a few transformations, which require a spherical sphere, the effect of F_0 is undone in matrix F_3. Parameter V_w is the volume of the myocardium of the LV. Waks et al. [1] obtained this volume by integrating in prolate spheroidal coordinates as shown in Equation (A.20)

$$a = \frac{\cos h\lambda}{\sin h\lambda} \tag{A.19}$$

$$V_w = \frac{\pi\delta^3}{4} \times (3(\cos h\lambda_0 - \cos h\lambda_i) + 4(\cos h^3\lambda_0 - \cos h^3\lambda_i)) \tag{A.20}$$

Bibliography

[1] E. Waks, J.L. Prince, and A.S. Douglas. Cardiac Motion Simulator for Tagged MRI. *Workshop on Mathematical Methods in Biomedical Image Analysis (NMBIA '96)*, page 0182, 1996.

[2] Frank H. Netter. *Atlas Of Human Anatomy*. Cambridge Studies In Comparati. Elsevier - Health Sciences Division, fifth edition, 2010.

[3] T. Arts, W.C. Hunter, A. Douglas, A.M.M. Muijtjens, and R.S. Reneman. Description of the Deformation of the Left Ventricle By A Kinematic Model. *Journal of Biomechanics*, 25(10):1119–1127, 1992.

[4] M. Nichols, N. Townsend, R. Luengo-Fernandez, J. Leal, A. Gray, P. Scarborough, and M. Rayner. European Cardiovascular Disease Statistics 2012. *European Heart Network, Brussels, European Society of Cardiology, Sophia Antipolis*, 2012.

[5] H. van Assen, L. Florack, A. Suinesiaputra, J. Westenberg, and B. ter Haar Romeny. Purely Evidence Based Multiscale Cardiac Tracking Using Optic Flow. *MICCAI 2007 workshop on CBM II*, pages 84–93, 2007.

[6] E.A. Zerhouni, D.M. Parish, W.J. Rogers, A. Yang, and E.P Shapiro. Human heart: tagging with MR imaging-a method for noninvasive assessment of myocardial motion. *Radiology*, 169(1):59–63, 1988.

[7] S.E. Fischer, G.C. McKinnon, S.E. Maier, and P. Boesiger. Improved Myocardial Tagging Contrast. *Magnetic Resonance in Medicine*, 30(2):191–200, 1993.

[8] N.F. Osman, W.S. Kerwin, E.R. McVeigh, and J.L. Prince. Cardiac Motion Tracking Using CINE Harmonic Phase (HARP) Magnetic Resonance Imaging. *Magnetic Resonance in Medicine*, 42(6):1048–1060, 1999.

[9] A.H. Aletras, S. Ding, R.S. Balaban, and H. Wen. DENSE: Displacement Encoding with Stimulated Echoes in Cardiac Functional MRI. *Journal of Computer Assisted Tomography*, 137:247–252, 1984.

[10] D. Bryant, J.A. Payne, D.N. Firmin, and D.B. Longmore. Measurement of flow with NMR imaging using gradient pulse and phase different technique. *Journal of Computer Assisted Tomography*, 8:588–593, 1984.

[11] J.L. Barron, D.J. Fleet, and S.S. Beauchemin. Performance of optical flow techniques. *International Journal of Computer Vision*, 12(1):43–77, 1994.

[12] B.K.P. Horn and B.G. Schunk. Determining Optic Flow. *Artificial Intelegence*, 17:185–203, 1981.

[13] L. Florack, W. Niessen, and M. Nielsen. The Intrinsic Structure of Optic Flow Incorporating Measurement Duality. *International Journal of Computer Vision*, 27(3):263–286, 1998.

[14] W.J. Niessen, J.S. Duncan, B.M. ter Haar Romeny, and M.A. Viergever. Spatiotemporal analysis of left ventricular motion. *Medical Imaging*, 95:192–203, February 1995.

[15] W.J. Niessen, J.S. Duncan, M. Nielsen, L.M.J. Florack, B.M. ter Haar Romeny, and M.A. Viergever. A multiscale approach to image sequence analysis. *Computer Vision and Image Understanding*, 65(2):259–268, February 1997.

[16] A. Suinesiaputra, L.M.J. Florack, J.J.M. Westenberg, B.M. ter Haar Romeny, J.H.C. Reiber, and B.P.F. Lelieveldt. Optic flow computation from cardiac MR tagging using a multiscale differential method - a comparative study with velocity encoded mri. *Proceedings of the Sixth International Conference in Medical Image Computing and Computer-Assisted Intervention-MICCAI 2003*, pages 483–490, November 2003.

[17] A. Manouras, A. Shala, E. Nykatari, K. Shahgaldi, R. Winter, P. Vardas, L. Brodin, and J. Nowak. Are measurements of systolic myocardial velocities and displacement with colour and spectral Tissue Doppler compatible? *Cardiovascular Ultrasound*, 7(29), June 2009.

[18] Bart M. ter Haar Romeny. *Front-End Vision and Multi-Scale Image Analysis*. Klumer Academic Publishers, first edition, 2003.

[19] D.S. Moore and G.P. McCabe. *Introdution to the Practice of Statistics*. New York: W.H.Freeman, third edition, 1999.

[20] W.A. Edelstein, P.A. Bottomley, and L.M. Pfeifer. A signal-to-noise calibration procedure for NMR imaging systems. *Med. Phys.*, 11(2):180–185, 1984.

[21] M.A. Bernstein, D.M. Thomasson, and W.H. Perman. Improved detectability in low signal-to-noise ratio magnetic resonance images by means of a phase-corrected real reconstruction. *Med. Phys.*, 15(5):813–817, 1989.

[22] H. Gudbjartsson and S. Patz. The Rician Distribution of Noisy MRI Data. *Magn. Reson. Med.*, 34(6):910–914, December 1995.

[23] Z. Ding and B.P. Lathi. *Modern Digital and Analog Communication Systems*. OXFORD UNIVERSITY PRESS, fourth edition, 2009.

[24] J. Prince and E. McVeigh. Motion Estimation from tagged MR image sequences. *IEEE Transactions on Medical Imaging*, 14(3):238–249, 1992.

[25] M.A. Brown and R.C. Semelka. MRI: Basic Principles and Applications. *ISBN-13: 978-0471433101*, page 94, Wiley-Liss, 3rd ed. 2003.